

70 Years of Chromospheric Solar Activity and Dynamics

Luca Bertello 6, Alexei A. Pevtsov 6, and Roger K. Ulrich 6

National Solar Observatory, 3665 Discovery Drive, Third Floor, Boulder, CO 80303, USA; Ibertello@nso.edu

Department of Physics and Astronomy, University of California, Los Angeles, 430 Portola Plaza, Los Angeles, CA 90095-1547, USA

Received 2020 March 31; revised 2020 May 9; accepted 2020 May 26; published 2020 July 16

Abstract

From 1915 to 1985 the monitoring program of the Mount Wilson Observatory, one of the Observatories of the Carnegie Institution of Washington, has taken over 35,000 daily images (spectroheliograms) of the Sun in the chromospheric resonance line of Ca II K. This important database constitutes a unique resource for a variety of retrospective analyses of the state of solar magnetism on multidecadal timescales. These observations may also hold the key for untangling some of the mysteries behind the solar dynamo, which in turn could result in a better predictive capability for current dynamo models. We describe here a procedure to calibrate and rescale these images so that homogeneous Carrington synoptic maps can be derived for the whole period covered by these observations. Temporal variations in full-disk chromospheric activity clearly show the signature of the 11 yr solar cycle, but no evidence is found for a statistically significant north/south hemispheric asymmetry. Using a feature-tracking technique we were also able to obtain the average solar rotation profile. We find no indication of any detectable periodicity in the temporal behavior of the orthogonalized rotation rate coefficients, suggesting the global chromospheric dynamics has not changed during the 70 years investigated in this work. We found also no significant evidence in our analysis for a hemispheric asymmetry in rotation rates.

Unified Astronomy Thesaurus concepts: Solar activity (1475)

1. Introduction

The Sun's variable magnetic fields constitute a rich source for processes that influence the heliosphere, and the Earth's upper atmosphere. The most prominent aspect of this variability is the solar cycle of activity, with a period of approximately 11 yr for the sunspot number and a period of about 22 yr for patterns of the magnetic polarity. The complex dynamo processes leading to the solar cycle of activity are now believed to arise from the boundary layer just below the solar convection zone known as the tachocline (Gilman 2000; Weiss & Tobias 2000).

The Mount Wilson solar photographic archive of the Carnegie Observatories makes available to the scientific community over 150,000 images of the Sun that were acquired over a time span in excess of 100 yr. The data include broadband images called white light directs, ionized CaK line spectroheliograms and hydrogen Balmer alpha spectroheliograms in two sets, one exposed for the disk and the other for the off-disk prominences. Peter Foukal recognized the importance of this archive in the late 1980s and carried out a digitization project. The digitization in the Foukal study was obtained with a system that yielded only 8 bits of transmitted intensity information over an array with an effective dimension of 512 \times 512, with the pixel size slightly unequal in two dimensions (Foukal 1996, 1998). Although the step wedge intensity information was recorded, it was not utilized during the reduction, due to the difficulty of automatically identifying the rectangles of constant illumination and then determining an appropriate photographic density from these rectangles. As a result, the primary data product from the Foukal study is the plage area determined by operator identification of plage boundaries. Conclusions from this study indicated that variations in the total solar irradiance are not large enough to influence global climate (Foukal & Milano 2001; Foukal et al. 2009).

In 2003, a new digitization project was initiated to maximize the scientific return of the archive. All of the Ca II K spectroheliograms series, which began in 1915 and ended in 1985, and about 50% of the white-light images, were digitized using an Eskographics F14 Scanmate scanner that provides about 12 bits of significant information. An additional set of Ca II K spectroheliograms obtained by Hale at the Kenwood Observatory during the years 1892–1894 is part of the collection but was not analyzed (Hale & Fox 1908). Extracted images, up to $3K \times 3K$ in size, were identified with original logbook parameters of observation time and scan format. The new images clearly reveal unprecedented details of the chromospheric network, allowing a variety of retrospective studies of the state of the solar magnetism and dynamics over a 70 yr temporal baseline.

In Bertello et al. (2010) the database was used as a benchmark to introduce a new approach to the calibration of Ca II K spectroheliogram images and to propose a different definition of the full-disk Ca II K plages and active network index. In this paper we take advantage of the multidecadal time span covered by this database to investigate two important aspects of solar variability: possible cycle variations and north—south hemispheric asymmetry in the profile of solar differential rotation and in chromospheric activity.

The study of solar differential rotation is crucial for understanding solar magnetic cycles and dynamo mechanisms. The combination of a solar rotation profile and the interaction between meridional circulation, the motion of flux tubes through the convection zone, and the generation of a magnetic field in the tachocline zone is believed to cause the solar activity cycle (Durney 2000; Ossendrijver 2003; Ruediger 2006; Miesch 2016). Presently, the Sun is the only star that provides the key to understanding how differential rotation is produced and the way in which the strength and periodicity of activity depend upon the latitude and depth variation of the differential rotation. The latitudinal profiles of the differential

rotation for other stars can be derived using a change in frequency of rotational modulation of the chromospheric activity as determined via the Fourier transform or periodogram analysis (e.g., Donahue & Baliunas 1992). Alternatively, it could also be determined by fitting the light curve with a model that has multiple spots with different rotation periods (e.g., Strassmeier & Bopp 1992). However, there are significant uncertainties in these determinations (e.g., Aigrain et al. 2015).

Historical databases are crucial for studying the long-term variations in solar differential rotation and the mechanisms that drive the solar cycle (Hathaway & Wilson 2004). Extensive studies of cycle-related variations of the solar-surface rotation have been conducted using mostly the extended Greenwich data set, consisting of positions of sunspot groups recorded between the years 1874 and 1981 (Brajša et al. 2006; Poljančić Beljan et al. 2017; Ruždjak et al. 2017).

Ca II K observations have been extensively investigated to characterize both the dynamics and morphology of chromospheric activity. Calibrated photographic Ca II K filtergrams obtained at the Schauinsland Observatory of the Kiepenheuer Institute Freiburg were used by Muenzer et al. (1989) to study the latitude dependency of chromospheric cells in quiet and active solar regions. A significant decrease of the cell size toward higher latitudes and an increase with locally increasing magnetic activity was found. A similar study by Brune & Woehl (1982) reported some evidence of a smaller size of polar cells compared to equatorial cells, by a factor of about 0.9. The existence of large-scale circulation patterns within the chromospheric network was investigated by Schroeter et al. (1978) and Schwan & Woehl (1978). In particular, the detailed study by Schroeter et al. (1978) indicates the presence of a single large cell with a \sim 40 m s⁻¹ radial outflow extending over more than 50° in longitude and statistically significant temporal changes in the differential rotation law that correlated with changes of meridional motions. Other techniques, such as tracings of bright Ca+-mottles, have also been commonly used to study properties of solar differential rotation, meridional flows, and giant circulation cells crossing the solar equator (Schroeter & Woehl 1975, 1976).

Other data have been used in the past for similar studies. For example, Li et al. (2013) studied solar-cycle-related variation of differential rotation using magnetic field data from the National Solar Observatory at Kitt Peak (USA) and the Solar and Heliospheric Observatory/MDI for the period 1976–2003 and found that the northern hemisphere rotates faster than the southern one at most times of the considered interval. Coronal bright point data have also been used to study the rotation of the solar corona (e.g., Karachik et al. 2006; Jurdana-Šepić et al. 2011; Sudar et al. 2015). Chromospheric plages, however, may offer some advantages in tracing solar rotation: they may persist longer than the corresponding sunspots and their number is typically larger. They are also spread over a larger range in latitude and are present at times when the number of sunspots is very limited. Unlike the coronal bright points, the chromospheric plages are not significantly elevated above the visible solar surface, and thus do not require a correction for the unknown height when using the image plane observations. Tracing individual sunspots may also complicate the determination of the differential rotation due to their proper motions, especially in emerging regions when the leading and following polarity spots may appear as moving away from each other (one would rotate faster and the other slower as compared with

the mean rotation rate for a given latitude). The rate of solar rotation can be determined as a function of time using the day-to day motions of plages visible in Ca II K images, as discussed in this study.

It is well documented that many classes of solar phenomena exhibit some form of hemispheric north-south asymmetry. The first evidence of such an asymmetry was reported by Spoerer (1889) based on observations showing that often, over long periods of time, more sunspots were found preferentially in one hemisphere. Strong asymmetries on the two hemispheres are not limited to the number of spots. For example, during the decade 1959-1969, the northern hemisphere showed a much larger number of faculae, prominences, and coronal brightness than the southern hemisphere (Waldmeier 1971). Most other solar activity indicators (e.g., sunspot areas, the number of flares, the flare index, radio bursts, coronal holes, CMEs, and solar wind) also manifest a strong asymmetry between the two hemispheres, with timescales that are not necessarily related to the sunspot (~11 yr) or magnetic (~22 yr) cycles of solar activity (Hathaway 2015; Chang 2018; Kramynin & Mikhalina 2018; Lekshmi et al. 2018; Javaraiah 2019). Hemispheric asymmetry may play an important role in determining the character of the solar cycle. Although the exact cause of this asymmetry is still unknown, it has been suggested that the random nature of the Babcock-Leighton process of poloidal field generation may play a significant role in producing this effect (Goel & Choudhuri 2009).

An important catalog of hemispheric sunspot numbers covering almost 60 yr (1945–2004) of observations from the Kanzelhöhe Solar Observatory (Austria) and the Skalnaté Pleso Observatory (Slovak Republic) was compiled by Temmer et al. (2006). In their investigation of the catalog it was found that the hemispheric asymmetry was significantly higher during periods of maximum solar activity, particularly during cycles 19 and 20, but no obvious systematic pattern could be connected to the 11 yr sunspot cycle and/or the 22 yr magnetic cycle.

Both solar differential rotation and hemispheric asymmetry are manifestations of physical processes that are linked to the nature of the solar dynamo. In this paper we analyze multiple decades of full-disk Ca II K observations to investigate possible variations in the solar rotation profile and differences in the global chromospheric activity between the two hemispheres over time. The next section describes the main steps involved in the data processing of the Ca II K images. Temporal variations in chromospheric activity are discussed in Section 3. In this section we briefly revisit the original definition of the Ca II K plage index given in Bertello et al. (2010) and compare the results with a more traditional definition of the plage index. Also described in this section is the procedure adopted to generate Ca II K synoptic maps for individual Carrington rotations covering the entire duration of the data set. Northsouth asymmetry in chromospheric activity is presented in Section 4. Derivation of an average solar differential rotation profile and its variations in time are discussed in Section 5. Analysis of a possible hemispheric asymmetry in rotation rates and conclusions are presented in Sections 6 and 7, respectively.

2. Data Analysis

2.1. Preprocessing, Calibration, and Image Selection

The database includes about 40,000 images acquired from 1915 August 10 to 1985 July 7 at the 60 foot solar tower at the

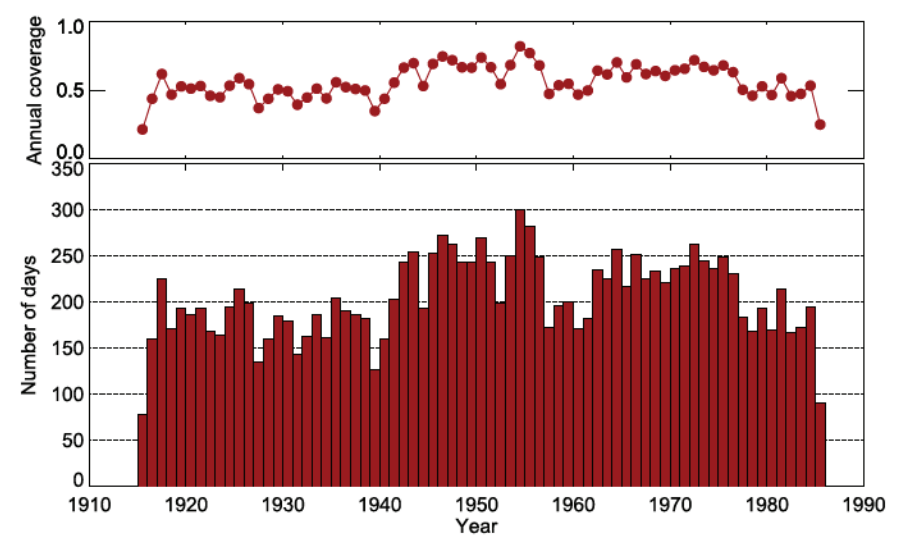


Figure 1. Year by year, number of days covered by at least one observation shown as a fraction of the year (top panel) and as total number of days (bottom).

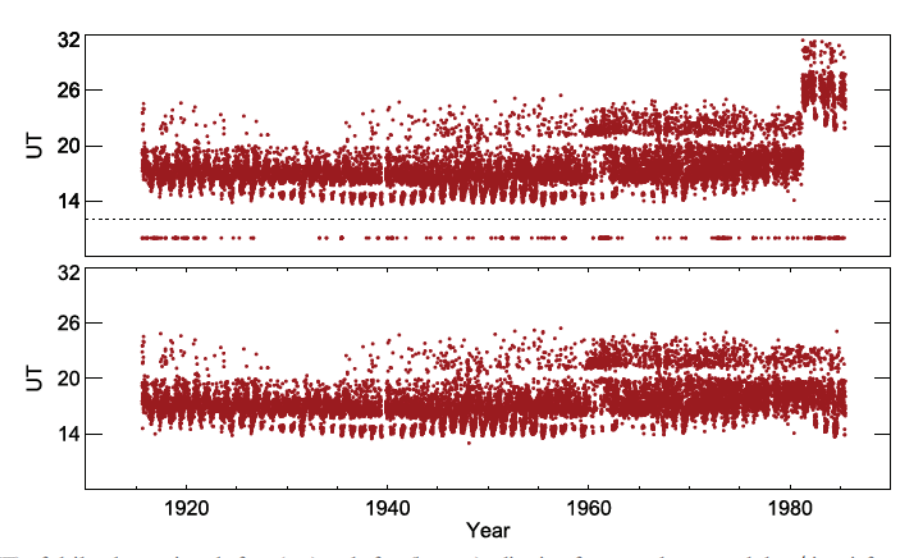


Figure 2. Universal time (UT) of daily observations before (top) and after (bottom) adjusting for wrongly reported date/time information into the FITS header of corresponding files. In the top panel, points below the dotted line correspond to adjustment in date (+1 day). Before 4/1/1981 MWO clocks were set to PST, then UT. This lead to a mistake while recording observation parameters from the original logbook.

Mount Wilson Observatory using the 13 foot (396.2 cm) spectrograph (Ellerman 1919). The spectrograph includes a folding flat mirror whose angle is adjustable but not documented to be 70° from the direction of the optical axis. The grating and this mirror are connected and both move when the grating is tilted. Multiple observations were taken most days, particularly before 1962. However, the quality of these images is not uniform across the database; rather, it varies quite significantly due to a number of factors, as discussed in Lefebvre et al. (2005) and Bertello et al. (2010). The quality of individual images is recorded based on two different metrics: (1) after visual inspection, a number between 1 and 4 is assigned to the image. Images with a value greater than 1 are deemed to be acceptable; and (2) the accuracy of the limb fit is also used to estimate the quality of an image, as described in Lefebvre et al. (2005). The image center and radius used here are the same as was originally determined. For the purposes of this work we decided to select only the best image for each day, based on the two metrics defined above. This reduces the total number of images investigated to 14,525. This number is rather uniformly distributed over the whole period covered by the

observations, with an annual coverage around 50% as shown in Figure 1. The images have then been flat-fielded following the same recipe given in Bertello et al. (2010).

2.2. Time and Date Correction

During the reinvestigation of the data set it was realized that the time stamp of a certain number of images, about 4%, was erroneously reported in the header of the corresponding original fits files. This issue was first discovered by Sheeley et al. (2011). The top panel of Figure 2 shows the universal time (UT) extracted from the header of those daily fits files. Clearly visible is the presence of at least four distinct large groups of values. Observations taken after 1981 April 1 show a systematic shift of 8 hr in UT, associated with the time difference between Pacific standard time (PST) and UT. Clocks at the Mount Wilson Observatory were set to PST before they were switched to UT at that particular date, and a mistake was made when reporting this time from the logbook of observations. There were also a few observations, shown below the horizontal dotted line in the top panel of Figure 2, for which the

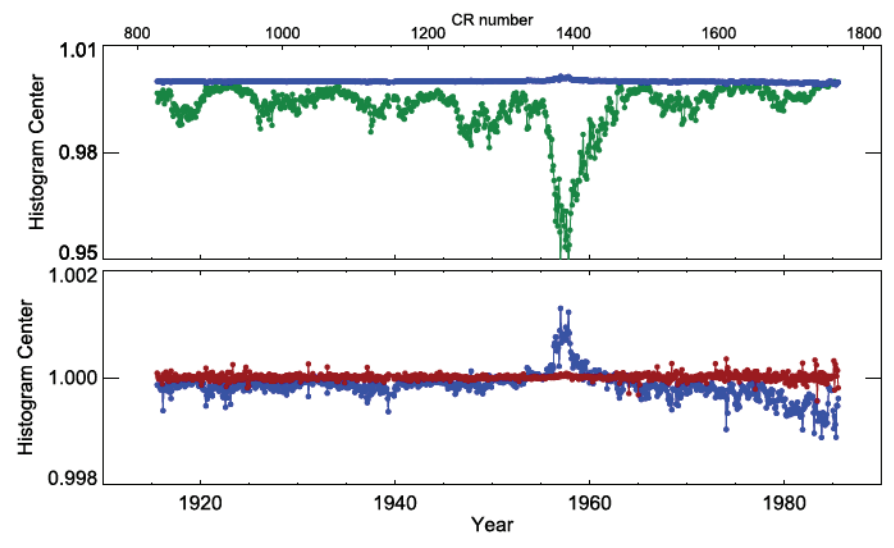


Figure 3. Average values, over Carrington numbers, of the histogram center parameter x_c before (green points) and after rescaling the images (blue and red points). The top panel shows the comparison between the results after flat-fielding (in green, no rescaling) and the first-pass rescaling (blue). The bottom panel shows the results of the second-pass rescaling (red) compared with the single-pass (blue). Note the change in scale between the two panels. Typical 1σ error bars are 5×10^{-4} (no rescaling), 4×10^{-5} (single-pass), and 3×10^{-5} for the double-pass.

date was off by 1 day. Both time and date have now been corrected in the latest version of the fits files.

The bottom panel shows the time series after those adjustments. It shows a couple of interesting features: (1) there is clearly a gap in the point distribution around 20 UT, corresponding to lunch breaks. It was customary that the cooks at the Mt. Wilson monastery served lunch at a very regular time and it was a sit-down affair. The 100 inch observer sat at the head of the table, other night people were on the east side, and the solar people on the west side. The 100 inch observer summoned the cooks with a bell. Regular attendees had wood napkin rings with their names engraved. This procedure lasted until Carnegie Observatories abandoned the Mt. Wilson site. (2) The other gap, around 15 UT, is likely related to the repositioning of the coelostat and it affects observations taken mostly between 1925 and 1965. Since the best seeing at the Observatory is typically early in the morning, there was a motivation to start observing soon after sunrise. When the Sun is low in the east, having the first flat also in the east requires a strongly oblique angle, so the observers probably put the first flat on the west side of the pillar for the second flat. As the Sun rises, the pillar and second flat will shade the first flat if it is in the west, so they would have to shift sides, producing the gap visible in the time series. The first flat was then shifted back to the west after noon when the pillar would again shade the first flat. The start time also shows clear annual variations, with observations starting earlier in summer and later in winter months.

2.3. Intensity Rescaling

As discussed in Bertello et al. (2010), the distribution of pixel values in flat-fielded images can be described by a four-parameter Gaussian function:

$$y(x) = A \exp(-u^2/2) + B,$$
 (1)

where $u = (x - x_c)/\sigma$, x is the bin value, and y is the fractional number of pixels in the solar disk with value x, while σ and x_c are the width and the center of the distribution, respectively. The distribution (histogram) is computed for x

values between 0.5 and 2.5, a bin size of 0.005, and using all pixels located within 0.98 solar radii from the center of the image.

The upper panels of Figures 3 and 4 show (in green) the derived time series for x_c and σ , respectively. The plot of x_c shows values around 1, as expected, but also a clear modulation with the cycle of solar activity. The amplitude of this modulation is of the order of 1%, but significantly larger during the period \sim 1955–1965 (cycle 19). A similar behavior, although less evident, is visible in the time series of σ . The most interesting feature of this figure is the increase in the value of σ during cycle 19. As explained in Bertello et al. (2010), the parameter σ is a measure of the plage contrast, and this increase during cycle 19 is likely due to to the exit slit of the spectrograph being narrower during that time. Associated with this change is an increase in the visibility of dark filaments, which are prominences projected against the photosphere that are typical of K3 images. A similar analysis conducted on Ca II K spectroheliograph data taken at the Kodaikanal Observatory does not reveal any significant change in the plage contrast for the same period (Tlatov et al. 2009).

This preliminary analysis shows that the flat-fielding alone does not produce a homogeneous set of calibrated images, where the distribution of the quiet Sun is identical for all images. To address this issue we have adopted the following double-pass rescaling approach:

$$I_n(x, y) = (\sigma_f / \sigma_{n-1})[I_{n-1}(x, y) - x_{c,n-1}] + 1 \quad (n = 1, 2),$$
(2)

where $I_0(x, y)$ and $I_2(x, y)$ are the original flat-fielded and final rescaled images, respectively. The constant σ_f is the final width of the distributions and was selected to have a value of 0.08. Plots of the $x_{c,n-1}$ and σ_{n-1} time series are shown in Figures 3 and 4. After the first iteration (n = 1), their temporal variability is already reduced significantly (blue points) compared to the results after the flat-fielding (green points). After the second and final iteration (red points, lower panels) both values of

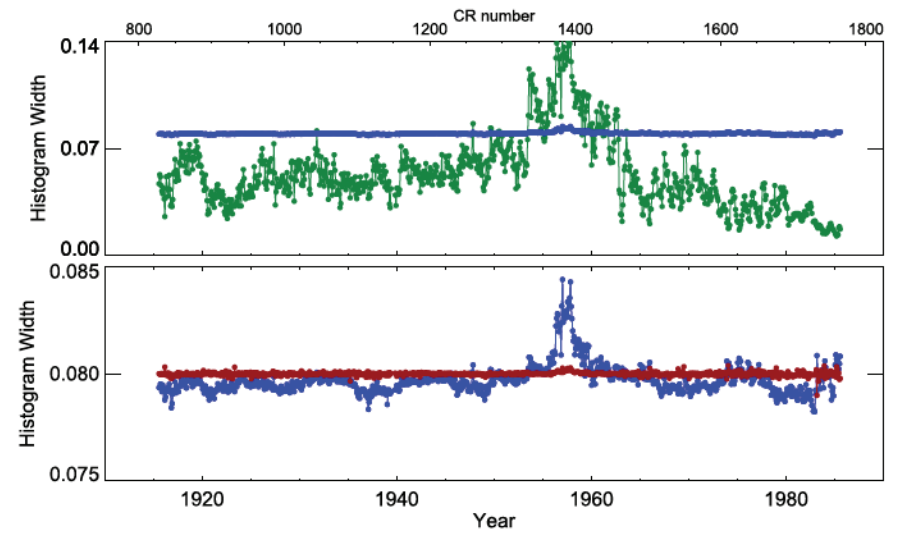


Figure 4. Same as Figure 3, but for histogram width parameter σ . Typical 1σ error bars are 3×10^{-3} (no rescaling), 8×10^{-5} (single-pass), and 4×10^{-5} for the double pass.

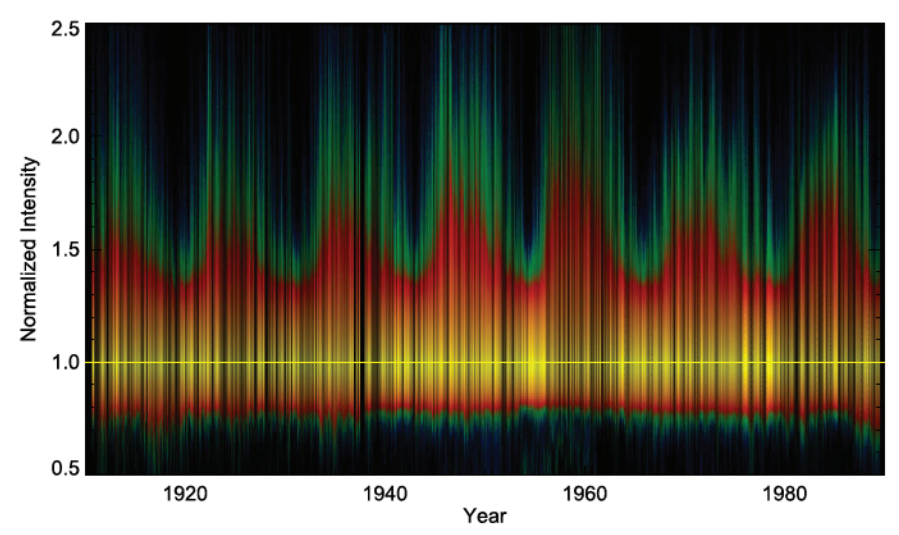


Figure 5. Two-dimensional histogram of normalized daily Ca II K intensity images after the two-pass rescaling method was applied (see the text). The horizontal yellow line corresponds to the location of the peak of the histogram. This image is shown at maximum contrast.

 $x_{c,n-1}$ and σ_{n-1} are nearly constant over the entire period covered by the observations, within a margin of less than 0.1%.

Figure 5 shows the 2D distribution of daily histograms after the rescaling. The 11 yr solar cycle modulation is clearly visible in this figure. It is characterized by the rise in the tail of the intensity distribution above ~ 1.2 , displayed as green and red regions, due to the increased contribution of plages and an active network. The central part of the distribution, representing the quiet chromospheric Sun and shown in yellow, is well defined and uniform.

2.4. Roll Angle Determination

Beginning 1935, polar marks indicating the solar north-south direction are present on most images and the roll angle can be easily calculated. However, a significant portion of the data set includes images without any mark, so in general the roll angle needs to be determined directly from the images. This can be achieved by cross-correlating consecutive images as described in Sheeley et al. (2011). Here we used their determination of the roll angle to transform the images into

solar heliographic latitude/longitude coordinates. We then cross-correlated the remapped images and adjusted the initial roll angle until only a shift in the east-west direction was detected. In general, our final determination of the roll angle agrees quite well with that by Sheeley et al. (2011), with discrepancies that are typically less than one degree. A good estimate of the roll angle is required for the construction of Carrington synoptic maps and for the determination of the solar differential rotation profile that are discussed in Sections 4 and 5. The result of the different steps involved in the correction of the Mount Wilson Ca II K images is shown in Figure 6, for three different days.

3. Chromospheric Activity: Temporal Variations

3.1. The Ca II K Plage Index

Several authors have used different definitions for the fulldisk Ca II K plage index. The most common approach is to define this index as the fractional area of the visible solar disk covered by plages. This requires a designation of different solar features based on intensities thresholds and/or areas. For

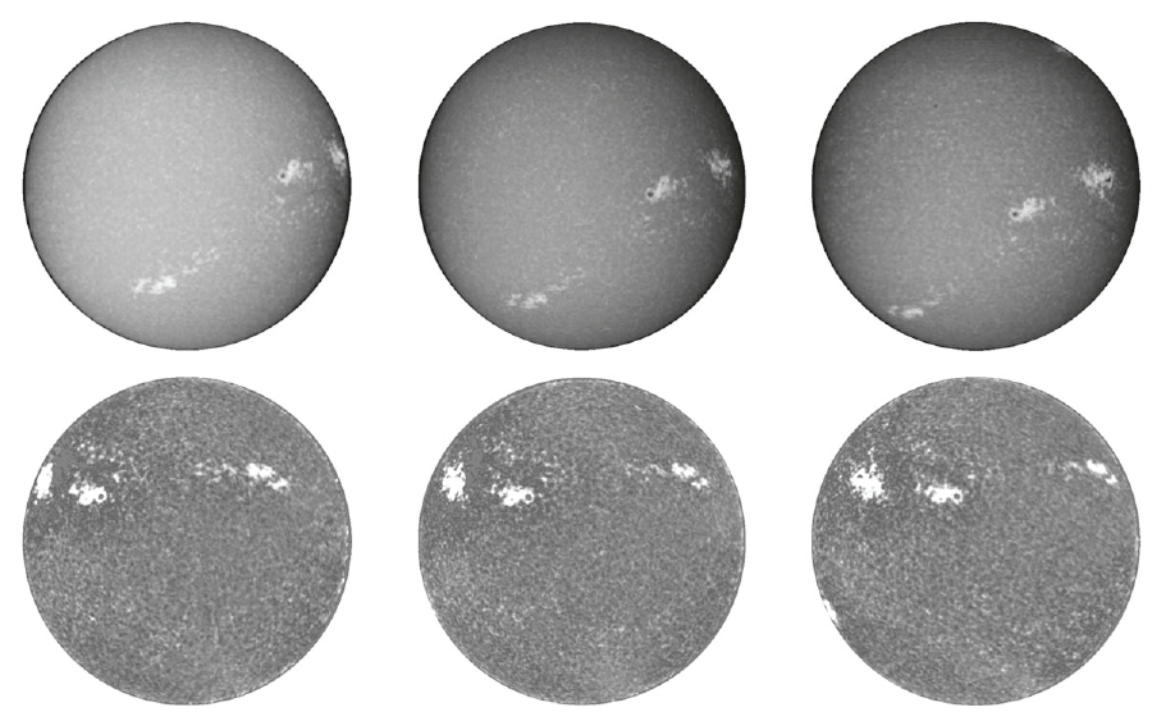


Figure 6. These solar images illustrate typical data for three consecutive days, 1924 November 18–20, and indicate the effect of our correction steps. The top three images are essentially unprocessed except for the removal of dust and pits. The bottom three images are flat field-corrected, rescaled, and roll angle-corrected (see text). The cross-correlation tracking of the daily motion of features visible on these images leads directly to the rotation rate results discussed in this paper.

example, in Priyal et al. (2017) solar features were classified in different groups that included enhanced network, active network, and two different types of plages. A similar classification was also used in Singh et al. (2018). In general, plage time series derived from different archives are in good agreement with each other (e.g., Chatzistergos et al. 2019), particularly at timescales longer than a month. However, some differences exist due not only to different properties and calibration of the images but also to the actual definition of the plage index itself.

Two different full-disk plage plus active network indices are introduced here. The first index is the value of the parameter B in Equation (1), first discussed in Bertello et al. (2010), after the double-pass rescaling is completed. It is important to note that the value of this parameter depends on the overall properties of the normalized intensity distribution across the image only, with the advantage that a prior and somewhat subjective classification of solar features is not required. The second index is defined as the ratio between the number of pixels in the visible hemisphere with rescaled intensity greater than $x_{c,1} + 2\sigma_1$ (see Equation (2)) and the total number of pixels in the disk. The choice of a 2σ threshold is based on the properties of the intensity distribution of those images. This distribution is typically Gaussian near its core (quiet Sun), but deviates from it at about 2σ when the contribution of pages becomes increasingly significant. Since $x_{c,1} \simeq 1$ and $\sigma_1 \simeq$ $\sigma_f = 0.08$, the intensity threshold is 1.16. Time series of the Carrington rotation averages of these two indices are shown in Figure 7. The agreement between the two series is excellent, indicating that these indices are virtually interchangeable in measuring global chromospheric activity at timescales longer than a Carrington rotation. As also shown in the figure, both time series correlate extremely well with the 13-month smoothed monthly total sunspot number provided by the World Data System sunspot Index and Long-term Solar

Observations (WDC-SILSO), Royal Observatory of Belgium, Brussels.

The only small difference between these two curves is at the end of cycle 21 (\sim 1984), where the values of the plage index determined from the fractional area (lower panel) are lower than the corresponding minimum determined from the parameter B (upper panel) compared to other minima.

3.2. Carrington Synoptic Maps

We have generated a full set of Ca II K integral synoptic maps, covering Carrington rotation 827-1764, using the rescaled and roll angle-corrected full-disk images discussed in Section 2. Each Carrington synoptic map includes all observations taken over a temporal window of about 40 days centered at the Carrington time corresponding to the middle of the map. To create the synoptic maps, daily images are first remapped into heliographic Carrington longitude and sine of latitude coordinates. A $\cos^3(L)$ taper is applied to the individual heliographic remapped images, where L is the central meridian distance. These remapped images are then shifted to the appropriate longitude in a regular 360 × 180 Carrington frame and merged together, following the procedure described in Bertello et al. (2014). This procedure identifies the pixels in the set of full-disk images that contribute to a given heliographic bin in the synoptic map and then computes their weighted average and standard deviation, resulting in two maps: the Ca II K synoptic map and the corresponding spatial standard deviation map. The spatial standard deviation map, as described in Bertello et al. (2014), is a measure of the statistical dispersion of all the pixel values contributing to a particular heliographic patch in the synoptic maps. It also accounts for more systematic changes related to evolution of features contributing to each patch. Note that the spatial variance is expected to be higher in areas associated with

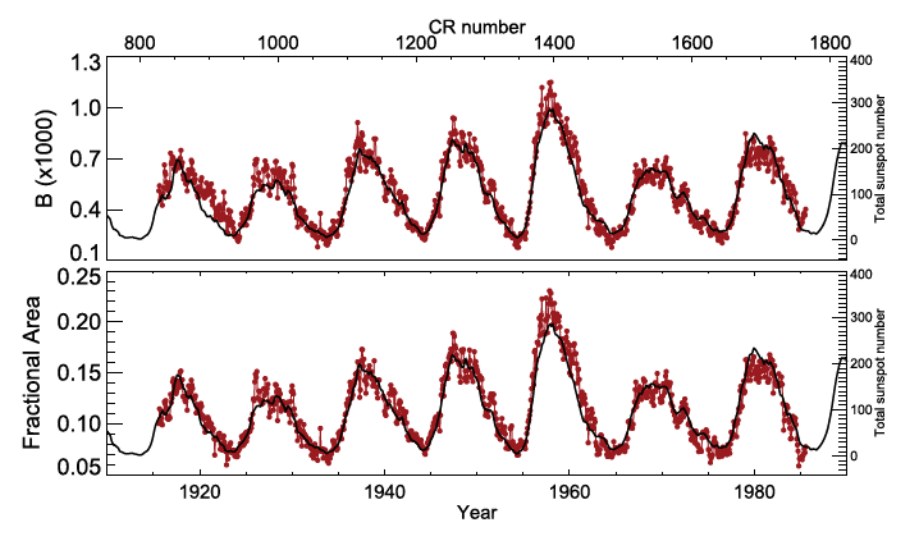


Figure 7. Carrington rotation averages derived from daily determinations of two different Ca II K plage plus active network indices. The top panel shows the index defined by the parameter *B* in Equation (1). The bottom panel shows the fraction of the visible solar hemisphere occupied by plages and an active network. Error bars are not shown for clarity, but their typical values are 0.018 and 0.003 (dimensionless) for the upper and lower time series, respectively. Shown in both panels is the behavior of the 13-month smoothed monthly total sunspot number (solid black line) from the WDC-SILSO, Royal Observatory of Belgium, Brussels.

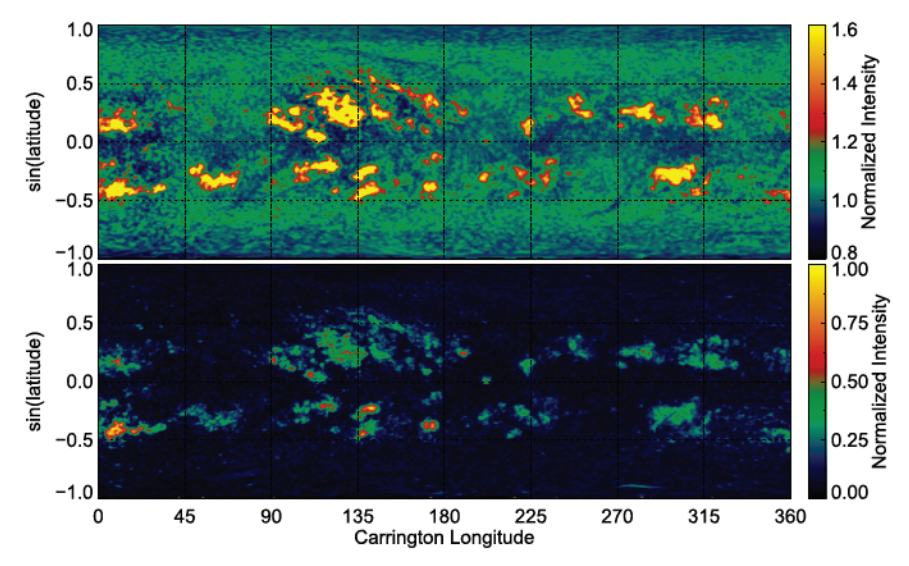


Figure 8. Synoptic map of Ca II K normalized intensity (top) for Carrington rotation 854 (1917 July-August) and corresponding standard deviation map (bottom). Yellow/red areas in the top map denote plage locations.

plages, making this map look somewhat similar to the weighted intensity map. Maps for selected Carrington rotation numbers are shown in Figures 8–10. They illustrate periods corresponding to different high levels of solar activity. Figures 8 and 9 show the Sun in Ca II K around the maximum of solar cycle 15 and during the decreasing phase of cycle 17 respectively. Figure 10 shows the level of chromospheric activity during the maximum of cycle 19, the most active cycle ever recorded. The presence of plages in these normalized intensity maps is clearly visible, as well as the presence of disk filaments. The standard deviation maps provide an estimate of the uncertainty associated with the normalized intensity maps.

A similar set of synoptic maps from the same Mount Wilson Ca II K images database was generated and extensively examined in Sheeley et al. (2011). Despite some differences in the normalization of those images, our maps show very similar properties, so we refer the reader to this previous study for an in-depth discussion of those maps.

Carrington synoptic maps are an excellent tool to examine the location and structure of individual active regions over a single Carrington rotation. However, for long-term studies of solar variability, a super-synoptic chart provides a better representation of the evolution of active regions (Ulrich et al. 2002). This chart is constructed by reversing the east-west direction of the individual synoptic maps so that the time is running forward, and placing them in chronological order. Figure 11 shows the result of this procedure. Clearly visible in this figure is the typical butterfly pattern representing the latitude drift of chromospheric activity during each solar cycle and the zone-leap at the time of beginning of new cycles. The annual modulation visible in the polar regions is due to the annual variations in the solar B-angle, and has not been corrected. Solar cycle 19 (1954–1964) is clearly the strongest cycle, with significant chromospheric activity extending to higher latitudes as compared to the other cycles. The supersynoptic chart shows a gradual progression of plages associated

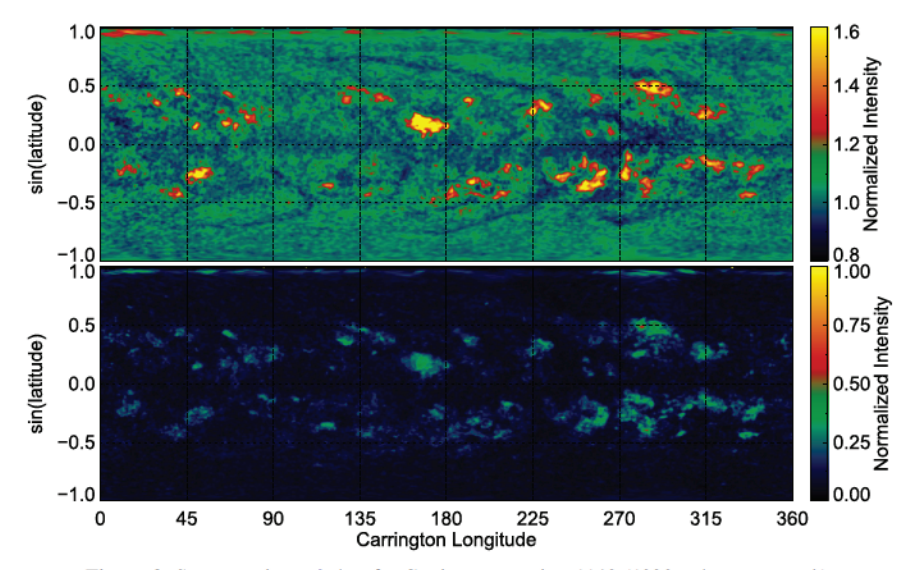


Figure 9. Same as Figure 8, but for Carrington rotation 1143 (1939 February-March).

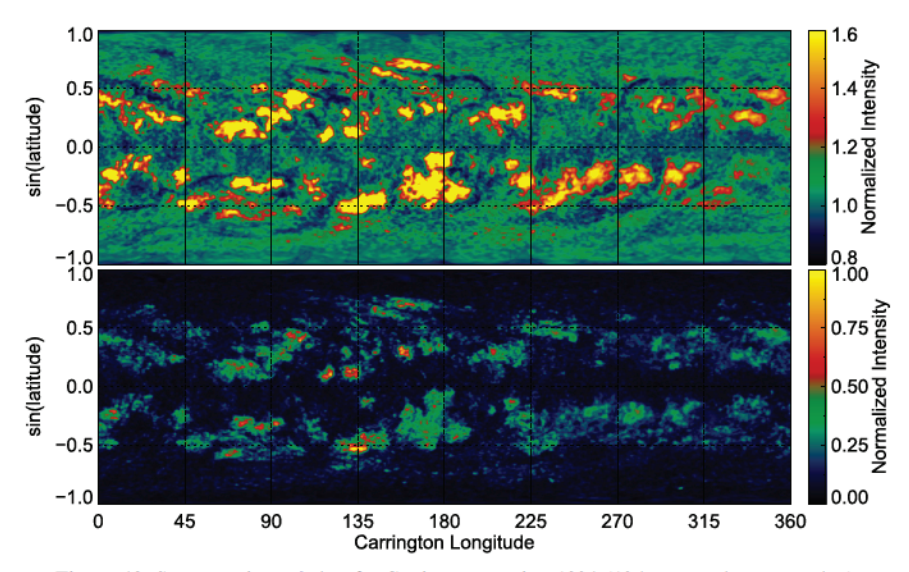


Figure 10. Same as Figure 8, but for Carrington rotation 1394 (1957 November-December).

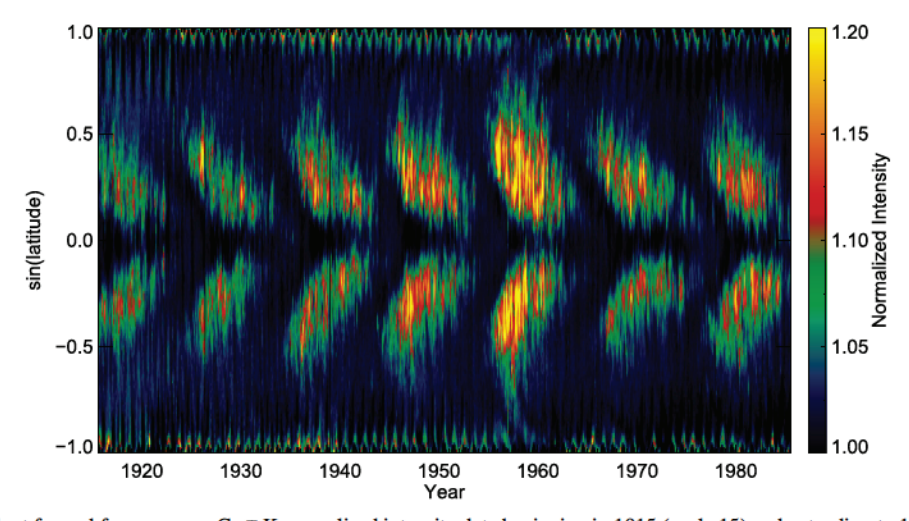


Figure 11. Super-synoptic chart formed from average Ca II K normalized intensity data beginning in 1915 (cycle 15) and extending to 1985 (cycle 22). No correction was applied to remove the modulation visible in the polar regions due to the annual variations in the solar B-angle.

with active regions from high latitude at the beginning of each cycle to the equator at the end of the cycle. It also shows the so-called rush-to-the-pole, a poleward drift of plages associated with a decaying active region. The best example of this drift is seen during cycle 19, from 1955 to 1960. This chart also shows the great level of uniformity in the individual synoptic maps achieved by our intensity rescaling of the daily Ca II K images.

4. Chromospheric Activity: North-South Asymmetry

The behavior of the solar activity in the northern and southern hemispheres has long been investigated, and it is known in general not to be symmetric. Although most studies have been focused primarily on properties of sunspots, many other indicators have been used: flares (e.g., Gao & Zhong 2016), filaments (e.g., Kong et al. 2015), polar faculae and plage region areas (e.g., Gonçalves et al. 2014), and magnetic fluxes (e.g., Hathaway & Upton 2016). Here we investigate the hemispheric properties of chromospheric features.

Differences in chromospheric activity between the north and south hemispheres can be investigated from the full set of synoptic maps used to produce the super-synoptic chart shown in Figure 11. For each hemisphere we have selected three different latitude bands, extending from the equator to about 25° and 50° , and from about 25° to 50° . For each band we then computed the average intensity value and corresponding standard deviation. The results are shown in Figure 12. Clearly visible is the signature of the 11 yr solar cycle of activity in all three latitude bands, with the lower band (below $\sim 25^{\circ}$) containing most of this variability.

It is also quite evident in Figure 12 that the activity levels in the two hemispheres track each other quite well over time, with no clearly pronounced asymmetry in the formation of chromospheric plages between the two hemispheres. This is confirmed by the results shown in the bottom panel, where the northsouth difference is computed together with the 99% confidence intervals. Figure 12, however, suggests a more complicated pattern. In the latitude band extending from the equator to about 25° (middle panel in the top figure) the northern hemisphere seems to lead the southern hemisphere by about 1–2 yr during cycles 17–19 (1930–1965). During cycles 20 and 21 this trend is reversed. In addition, the decreasing phase of cycle 19 (1957–62) shows a slightly more active northern hemisphere. However, these patterns are well within the 99% confidence levels shown at the bottom of Figure 12.

The lack of a strong hemispheric asymmetry as derived from the analysis of the MWO database of Ca II K spectroheliograms may suggest a difference in the behavior between stronger (sunspot) and weaker (plages) magnetic field regions during different phases of the solar cycle.

5. Chromospheric Rotation: Temporal Variations

The rate of solar rotation over the whole solar surface can be determined as a function of time using the day-to-day motion of solar features. The details of the adopted procedure are given below:

 Each individual full-disk Ca II K image is remapped and interpolated into a new 720 × 720 grid of equal heliographic 0°.25 longitude-interval and latitude-interval.

- 2. Consecutive remapped images (*I*) in the sequence are grouped in pairs $\{(I_i, I_{i+1}) \mid i = 1,...,N\}$, where *N* is the total number of images in the sequence.
- 3. If the time separation (Δt) between two images in the pair is greater than 4 days, then the pair is removed from the analysis. Longer gaps between consecutive observations typically produce a negligible correlation. With this limit, about 13,400 pairs of observations are available from the entire database.
- 4. For the selected pairs, the pattern of rotation rate is then determined by cross-correlating 11 separated latitude zones spanning the solar disk between ±50° in latitude, and limited to the central region between ±60° in longitude only. In general, the correlation is higher during periods of high solar activity and for observations separated in time by only a few days.

For each zone, the synodic rotation rate $\omega_{\text{syn}}(\phi)$ is given by:

$$\omega_{\text{syn}}(\phi) = 0.2020[\Delta L(\phi)]_{\text{max}} / \Delta t \text{ (μrad s}^{-1}), \tag{3}$$

where $[\Delta L(\phi)]_{\rm max}$ is the value of the longitude lag (in degrees) with the maximum correlation, ϕ is the latitude, and 0.2020 is the conversion factor from deg day⁻¹ to $\mu {\rm rad~s}^{-1}$. The transformation from synodic to sidereal rotation velocities of the Sun is given by

$$\omega_{\rm sid} = \omega_{\rm syn} + \frac{\bar{\omega}_{\rm Earth}}{r} \frac{\cos^2 \Psi}{\cos i},\tag{4}$$

where $\bar{\omega}_{\rm Earth} = 0.1991~\mu~{\rm rad\,s^{-1}}$ (0.9856 deg day⁻¹), r is the dimensionless Earth–Sun distance in astronomical units (au), i is the inclination of the solar equator to the ecliptic, and Ψ is the angle between the pole of the ecliptic and the solar rotation axis (Skokić et al. 2014). However, this level of precision is not required here, and we simply used the approximation $\omega_{\rm sid} = \omega_{\rm syn} + \bar{\omega}_{\rm Earth}$.

For each latitude band an outlier-resistant mean and standard deviation is computed using a 2σ cutoff from the median. We assume the following functional form for the latitude dependence of the solar angular rotation:

$$\omega_{\rm sid}(\phi) = A + B\sin^2(\phi) + C\sin^4(\phi),\tag{5}$$

where the three coefficients $\{A, B, C\}$ can be obtained from a least-squares fit to the data. The following sidereal values for the coefficients are determined:

$$A = 2.8860 \pm 0.0005 \ \mu \text{rad s}^{-1} \ B = -0.4299 \pm 0.0071 \ \mu \text{rad s}^{-1}$$

$$C = -0.4525 \pm 0.0159 \ \mu \text{rad s}^{-1}.$$

The A coefficient gives the rotation rate at the solar equator, while the other two coefficients provide the latitude dependency. Both mean rotation rate values for each latitude band and our best-fit model are shown in Figure 13.

The agreement between the model and the data is excellent. Measurements of solar differential rotation have been published in several studies, using different techniques and leading to different results. A comparison of rotation measurements from Doppler shift, Doppler feature-tracking, magnetic feature tracking, and p-mode splittings was compiled by Beck (2000). In a more recent study, Lamb (2017) achieved high-precision measurements of solar rotation by tracking the motions of individual magnetic features from a single month of SDO/HMI observations. In Table 1, we compare our results

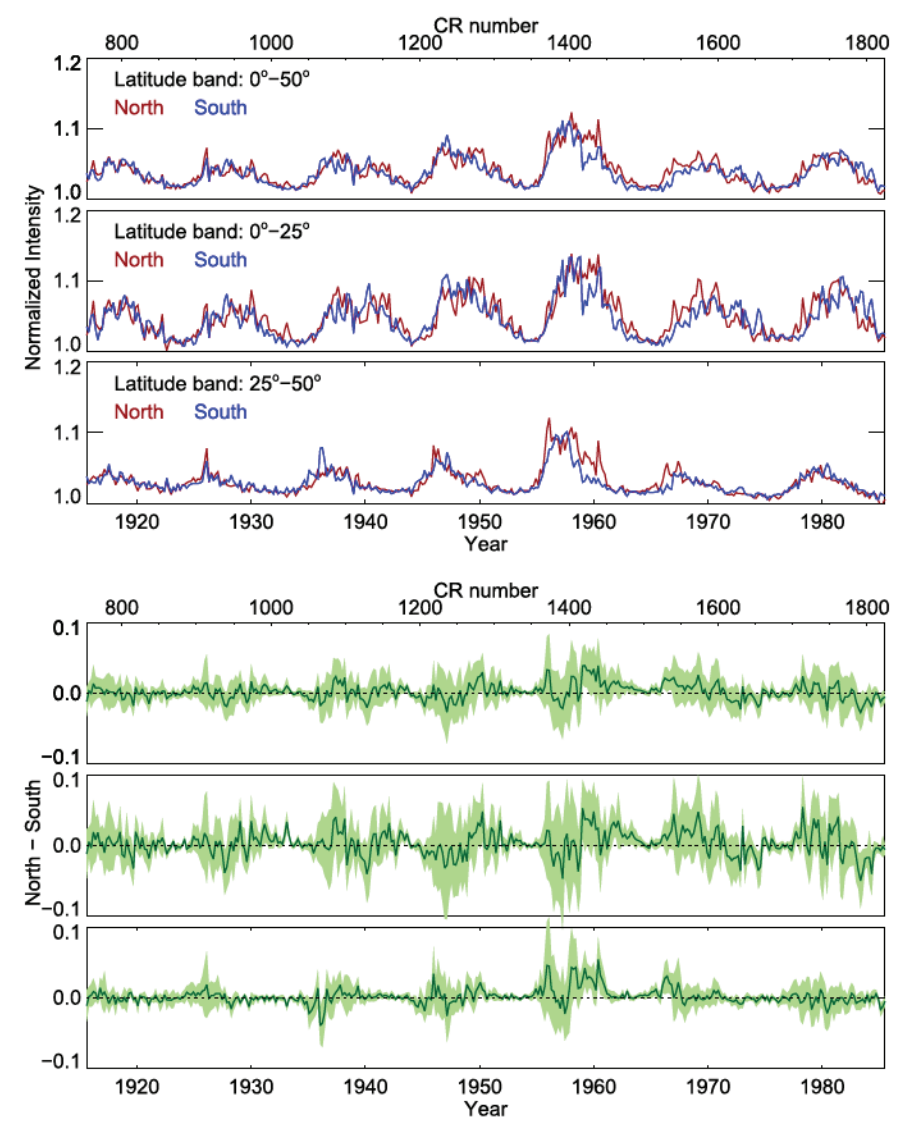


Figure 12. Hemispheric north-south chromospheric activity. Average normalized intensities, for the three different latitude bands indicated in the top figure, are shown for both the north (red curves) and south (blue curves) hemispheres. The corresponding differences, including the 99% confidence interval indicated by the green region, are shown in the bottom figure.

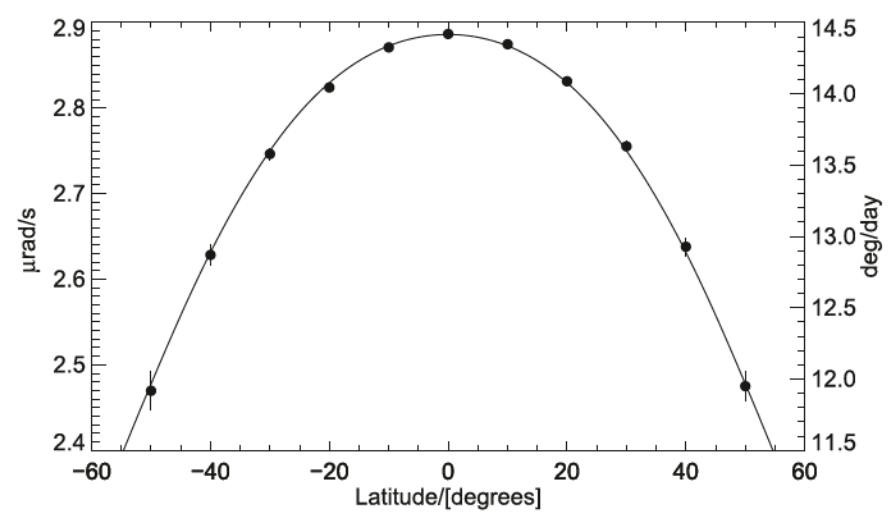


Figure 13. Average sidereal solar rotation rate profile as a function of latitude determined from more than 13,400 observations taken in the Ca II K spectral line during the period 1915–1985. Error bars are 5σ , and the best fit to the data (solid curve) is given by $2.8860 - 0.4299 \sin^2(\phi) - 0.4525 \sin^4(\phi)$, where ϕ is latitude (Equation (5)).

Table 1
Measurements of Sidereal Solar Rotation Rate

Source	$A = (\mu \text{rad s}^{-1})$	$\frac{B}{(\mu \text{rad s}^{-1})}$	C (μ rad s ⁻¹)
Beck (2000) (Table I)	2.844 ± 0.035	-0.351 ± 0.038	-0.478 ± 0.056
Beck (2000) (Table II)	2.921 ± 0.031	-0.531 ± 0.103	-0.422 ± 0.062
Lamb (2017) This work	$\begin{array}{c} 2.888 \pm 0.001 \\ 2.886 \pm 0.001 \end{array}$	-0.373 ± 0.011 -0.430 ± 0.007	$\begin{array}{c} -0.528 \pm 0.019 \\ -0.453 \pm 0.016 \end{array}$

Note. Table I in Beck (2000) includes results of spectroscopic rotation measurements obtained from 10 different studies, while Table II lists results using tracer rotation techniques from 14 separated studies. We computed and show here the average values from each table, and the corresponding standard deviation. The published original values in Lamb (2017) have been converted to μ rad s⁻¹.

with those published in these two studies. The two tables in Beck (2000) provide a list of rotation measurements obtained using either spectroscopic (Table I) or tracer techniques (Table II). For our comparison we have averaged the values in these two tables separately.

The values A for three of the four entries in Table 1 indicate no significant trend in equatorial rotation rate between photospheric and chromospheric layers, while the higher equatorial rotation value (2.921 μ rad s⁻¹) obtained by tracking mostly sunspots has been long established. A close comparison between our results and those from Lamb (2017) suggests a slightly different behavior in the latitude dependency of the solar rotation profile (coefficients B and C). While the two equatorial rate values are within 1σ , the difference in the B and C coefficients seems to suggest a slight decrease in rotation rate (\sim 0.02 μ rad s⁻¹) between the photosphere and low chromosphere at latitudes between \sim 30° and \sim 60°.

The two coefficients B and C are almost the same in magnitude and sign, suggesting a partial dependence between them. This dependence was first identified by Snodgrass & Howard (1985) in a study of Doppler features in the solar photosphere. As suggested in their work, the cross0talk in the fit coefficients can be eliminated by orthogonalizing the fit, that is:

$$\omega_{\text{sid}}(\phi) = \bar{A} + \bar{B}T_2^1(\sin\phi) + \bar{C}T_4^1(\sin\phi), \tag{6}$$

where T_j^i are the Gegenbauer polynomials. Since the T's are a linear combination of $\sin^2(\phi)$ and $\sin^4(\phi)$, the new set of coefficients is also a linear combination of the original set. The relationship between new and old coefficients is given by:

$$\bar{A} = A + \frac{1}{5}B + \frac{3}{35}C = 2.761 \pm 0.002 \,\mu\text{rad s}^{-1}$$

$$\bar{B} = \frac{1}{5}B + \frac{2}{15}C = -0.146 \pm 0.002 \,\mu\text{rad s}^{-1}$$

$$\bar{C} = \frac{1}{21}C = -0.022 \pm 0.001 \,\mu\text{rad s}^{-1}.$$
(7)

As discussed in Snodgrass & Ulrich (1990), this set of orthogonal coefficients is a more suitable choice when investigating time variations in the solar rotation profile. For this purpose we have segmented our database into 5 yr long subsets with a 50% overlap, and computed the value of the orthogonal coefficients for each subset. The result is shown in

Figure 14. There is no indication of any significant periodicity in the temporal behavior of the orthogonalized rotation rate coefficients over the 60 yr investigated in this work, suggesting that the chromospheric solar differential rotation profile remained mostly constant during the twentieth century.

A similar figure for the set of coefficients $\{A, B, C\}$, not included in this paper, shows a clear anti-correlation between the B and C coefficients and a \sim 40 yr periodicity in the A coefficient. This suggests that any long-term periodicities in solar rotation found using non-orthogonalized coefficients need to be treated with caution.

6. Chromospheric Rotation: North-South Asymmetry

An analysis similar to the one used to derive the results shown in Figure 13 can be performed to investigate possible hemispheric asymmetries over time in the chromospheric rotation profile. For this purpose we separated the rotation rate values derived from the 13,400 pairs of selected observations into two groups: one group containing the values for the five latitude bands in the northern hemisphere, and a second group containing the values for the corresponding five southern latitudes. For each latitude band we segmented the data set into a sequence of 5 yr long subsets with a 50% overlap, and computed for each subset the outlier-resistant mean with a 2σ cutoff. Finally, we have subtracted from these final values the average profile given by Equation (5) (Figure 13) to create time series of solar rotation rate residuals.

Figure 15 shows the time dependency of rotation rate residuals for each hemisphere separately, and for the five latitude bands investigated in this study. At low latitudes, below 40° , there is no significant difference in the rate of rotation between the northern and southern hemispheres. There are also no particular trends that can be detected. At higher latitudes the results are more difficult to interpret, with some indication at times of a possible north–south asymmetry and long-term variations in the rotation rate. The amplitude of these long-term variations seems to increase with latitude, and is quite evident within the 50° latitude bands. This might suggest some non-solar effect, as the uncertainty on these data also increases with the latitude. The largest discrepancy in rotation rate between the two hemispheres is seen at about 4° , between ~ 1945 and ~ 1957 .

These results are also confirmed by taking the simple difference of the mean rates of solar rotation between the two hemispheres (north minus south values), as shown in Figure 16. A possible north–south asymmetry, at a 3σ level, is only visible for short periods of time at intermediate latitudes (between 30° and 40°) during the late 1940s and early 1950s. These results, however, are not consistently significant to provide a conclusive answer for the existence of a north–south asymmetry in the chromospheric rotation rate.

7. Conclusions

In this study we have analyzed more than 14,000 individual daily spectroheliograms of the Sun extracted from the database of the monitoring program of the Mount Wilson Observatory. The images investigated in this work were taken in the chromospheric resonance line of Ca II K and cover the period from 1915 August to 1985 July. The improved processing and calibration of those spectroheliograms with respect to previous studies has allowed us to address several important questions

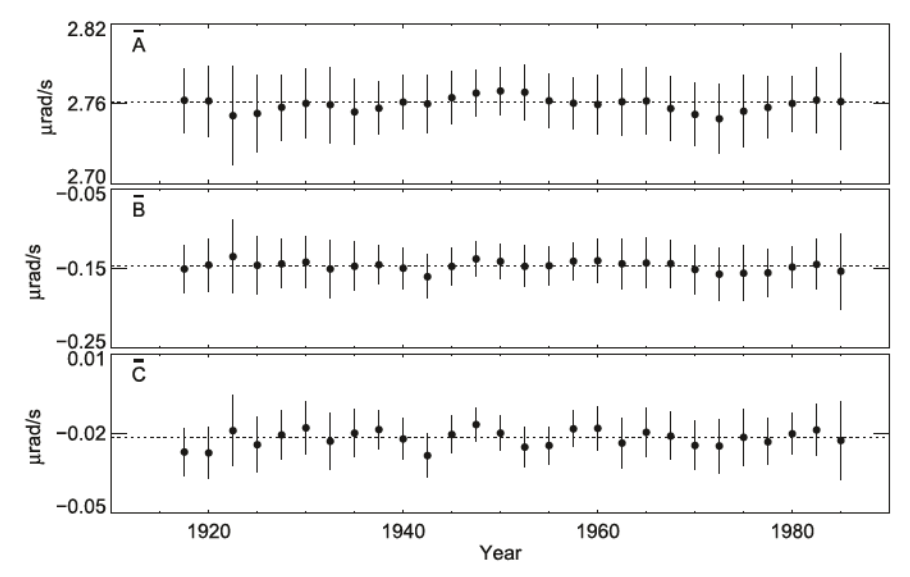


Figure 14. Time variation in the orthogonal coefficients. Coefficients were computed using Equations (5) and (7). Observations were grouped in 5 yr intervals, with a 50% overlap. The error bars are 3σ formal standard errors returned from the curve fit, while the horizontal dotted lines are the values (Equation (7)) obtained from fitting the entire data set.

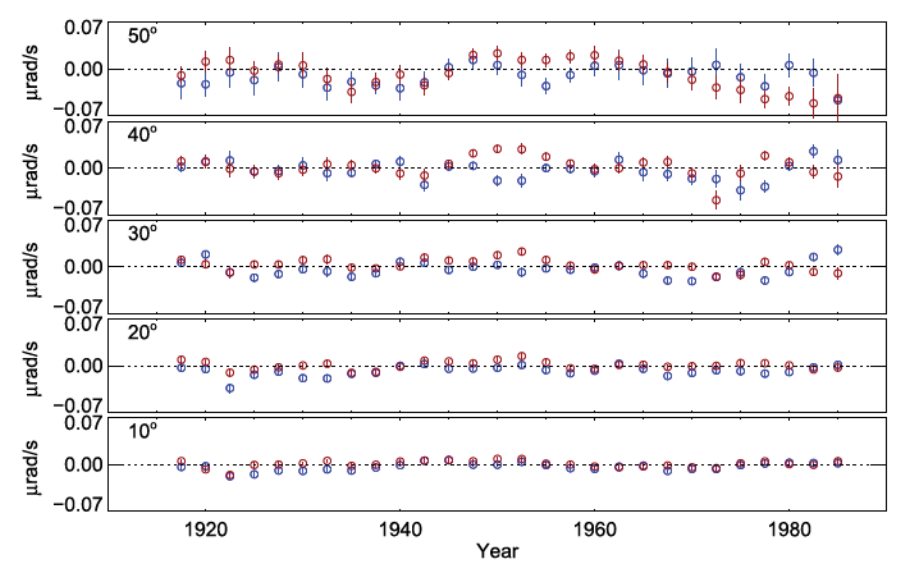


Figure 15. Time dependency of the mean rotation rate deviation from the average profile given by Equation (5) as a function of latitude. Northern hemisphere mean values are indicated by open red circles, while the southern values are shown as open blue circles. Error bars are the 1σ standard deviation of the mean. Mean values are computed over a 5 yr time span, with a 50% overlap.

related to the long-term variability in the Sun's chromospheric emission. (1) How is the chromospheric emission modulated by the solar cycle? (2) Does the Sun's chromospheric rotation profile vary with the cycle? (3) Does the distribution of plages across the solar disk show a hemispheric preference with time?

The annual coverage of the daily images investigated in this work is quite uniform, with a typical duty cycle at around 50% over the entire 1915–1985 time frame. During the analysis of these images we discovered and corrected an error in the time stamp reported in the header of the original fits files, mostly affecting observations taken after 1981 April. A major challenge in processing historical observations covering multiple solar cycles is the ability to produce an archive of homogeneously calibrated images. This is particularly important when long-term properties of the data set need to be investigated. In our study we have implemented a new procedure to effectively calibrate Ca II K intensity images.

The procedure, a double-pass rescaling, has proven to be very effective at producing a homogeneous set of calibrated images. From the rescaled images we have defined two separate plage indices, matching each other very well, and produced sets of Carrington synoptic maps covering the entire period under investigation. Our Ca II K emission indices clearly show the signature of the different cycles of activity, with cycle 19 being the most active recorded.

Somewhat surprisingly, we have not detected significant variations in both the solar rotation profile and the north-south hemispheric distribution of chromospheric activity during most of the twentieth century. Long-term variations in solar differential rotation have been investigated by several authors using different tracers, with somewhat contradictory results. For example, using sunspot group data and the daily values of the equatorial rotation rate derived from the Mt. Wilson Doppler measurements, Li et al. (2014) found that the

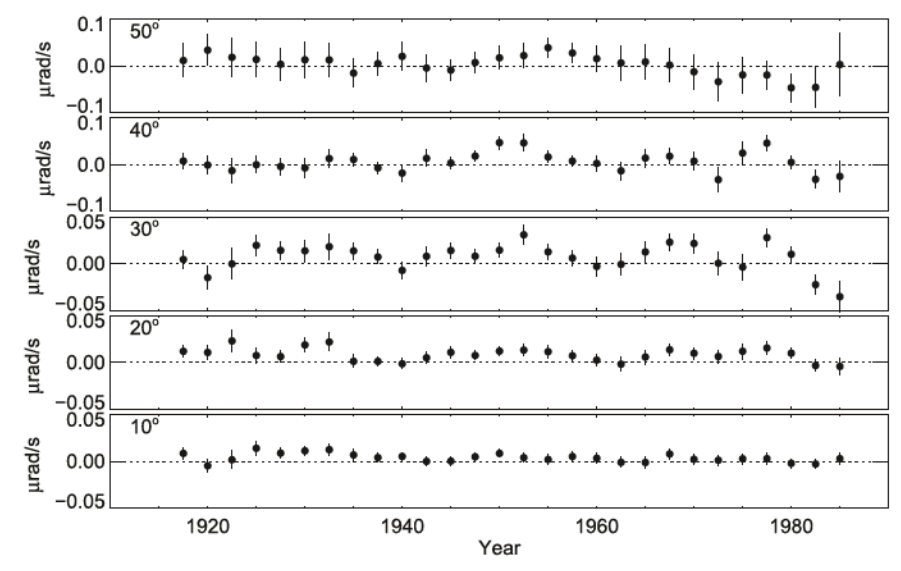


Figure 16. Time dependency of the difference between the northern and southern mean rotation rates as a function of latitude. As in Figure 15, mean values are computed over a 5 yr time span, with a 50% overlap. Errors bars are the 1σ standard deviation of the difference.

solar-surface rotation rate at the equator shows a secular decrease of about $1-1.5 \times 10^{-3}$ deg day $^{-1}$ yr $^{-1}$ since cycle 12 onward, but not significant variations in latitude. On the other hand, Heristchi & Mouradian (2009) found consistent results between the rotation rates determined from time series of the sunspot numbers and the flux of the corona at 2800 MHz, with a periodicity of about 52 yr and no difference between the northem and southern hemisphere rotation rates. In addition, studies of the rotation of active longitudes of sunspots for the past 12 solar cycles suggest that the long-term evolution of the solar surface rotation has a quasi-periodicity of about 80–90 yr, with some indications of hemispheric asymmetry (Zhang et al. 2013; Suzuki 2014).

Our analysis raises questions about the validity of long-term quasi-periodicity in the solar rotation. While the original coefficients in the solar rotation profile do show a 40 yr periodicity, it disappears when we use orthogonalized coefficients to reduce the cross-talk between those coefficients. A clear hemispheric asymmetry in both solar chromospheric activity and rotation is also absent in our data. Continuous and consistent observations of solar phenomena over multiple decades are fundamental for understanding the underlying physical mechanisms responsible for the observed variations in the Sun's magnetic activity. With the significant progress made over the past decade in the development of more sophisticated numerical and physical models of the solar dynamo, the importance of these observations becomes even more critical. Observations play a key role in constraining and validating these models. While the properties of solar photospheric features such as sunspots have long been used to characterize the solar cycle of activity, systematic studies of chromospheric activity and dynamics have been somewhat more limited. The main purpose of this paper is to supplement previous studies by providing a comprehensive picture of the solar chromosphere by exploiting the properties of a unique database covering 70 yr of observations.

The data set is available under doi:10.7910/DVN/RQSEJ8. L.B. and A.A.P. are members of the international team on Reconstructing Solar and Heliospheric Magnetic Field Evolution Over the Past Century supported by the International

Space Science Institute (ISSI), Bern, Switzerland. The National Solar Observatory (NSO) is operated by the Association of Universities for Research in Astronomy (AURA), Inc., under cooperative agreement with the National Science Foundation. Observations at the Mount Wilson Observatory have been supported over the years by the Carnegie Institute of Washington, the National Aeronautic and Space Agency, the US National Science Foundation, and the US Office of Naval Research. sunspot data from the World Data Center SILSO, Royal Observatory of Belgium, Brussels.

Facility: MtW:46 m solar tower.

ORCID iDs

Luca Bertello https://orcid.org/0000-0002-1155-7141
Alexei A. Pevtsov https://orcid.org/0000-0003-0489-0920
Roger K. Ulrich https://orcid.org/0000-0003-4041-4657

References

```
Aigrain, S., Llama, J., Ceillier, T., et al. 2015, MNRAS, 450, 3211
Beck, J. G. 2000, SoPh, 191, 47
Bertello, L., Pevtsov, A. A., Petrie, G. J. D., & Keys, D. 2014, SoPh, 289, 2419
Bertello, L., Ulrich, R. K., & Boyden, J. E. 2010, SoPh, 264, 31
Brajša, R., Ruždjak, D., & Wöhl, H. 2006, SoPh, 237, 365
Brune, R., & Woehl, H. 1982, SoPh, 75, 75
Chang, H.-Y. 2018, JASS, 35, 55
Chatzistergos, T., Ermolli, I., Krivova, N. A., & Solanki, S. K. 2019, A&A,
   625, A69
Donahue, R. A., & Baliunas, S. L. 1992, ApJL, 393, L63
Durney, B. R. 2000, SoPh, 197, 215
Ellerman, F. 1919, PASP, 31, 16
Foukal, P. 1996, GeoRL, 23, 2169
Foukal, P. 1998, GeoRL, 25, 2909
Foukal, P., Bertello, L., Livingston, W. C., et al. 2009, SoPh, 255, 229
Foukal, P., & Milano, L. 2001, GeoRL, 28, 883
Gao, P. X., & Zhong, J. 2016, NewA, 43, 91
Gilman, P. A. 2000, SoPh, 192, 27
Goel, A., & Choudhuri, A. R. 2009, RAA, 9, 115
Gonçalves, E., Mendes-Lopes, N., Dorotovič, I., Fernandes, J. M., &
   Garcia, A. 2014, SoPh, 289, 2283
Hale, G. E., & Fox, P. 1908, The Rotation Period of the Sun as Determined
   from the Motions of the Calcium Flocculi (Washington, DC: The Carnegie
  Institution of Washington)
```

Hathaway, D. H. 2015, LRSP, 12, 4

Hathaway, D. H., & Upton, L. A. 2016, JGRA, 121, 10,744

```
Hathaway, D. H., & Wilson, R. M. 2004, SoPh, 224, 5
Heristchi, D., & Mouradian, Z. 2009, A&A, 497, 835
Javaraiah, J. 2019, SoPh, 294, 64
Jurdana-Šepić, R., Brajša, R., Wöhl, H., et al. 2011, A&A, 534, A17
Karachik, N., Pevtsov, A. A., & Sattarov, I. 2006, ApJ, 642, 562
Kong, D.-F., Qu, Z.-N., & Guo, Q.-L. 2015, RAA, 15, 77
Kramynin, A. P., & Mikhalina, F. A. 2018, Ge&Ae, 58, 937
Lamb, D. A. 2017, ApJ, 836, 10
Lefebvre, S., Ulrich, R. K., Webster, L. S., et al. 2005, MmSAI, 76, 862
Lekshmi, B., Nandy, D., & Antia, H. M. 2018, ApJ, 861, 121
Li, K. J., Feng, W., Shi, X. J., et al. 2014, SoPh, 289, 759
Li, K. J., Shi, X. J., Xie, J. L., et al. 2013, MNRAS, 433, 521
Miesch, M. S. 2016, AdSpR, 58, 1453
Muenzer, H., Schroeter, E. H., Woehl, H., & Hanslmeier, A. 1989, A&A,
  213, 431
Ossendrijver, M. 2003, A&ARv, 11, 287
Poljančić Beljan, I., Jurdana-Šepić, R., Brajša, R., et al. 2017, A&A, 606, A72
Priyal, M., Singh, J., Belur, R., & Rathina, S. K. 2017, SoPh, 292, 85
Ruediger, G. 2006, in IAU Joint Discussion 26, Solar and Stellar Activity
   Cycles (Prague, Czech Republic), 72
Ruždjak, D., Brajša, R., Sudar, D., Skokić, I., & Poljančić Beljan, I. 2017,
   SoPh, 292, 179
```

```
Schroeter, E. H., & Woehl, H. 1975, SoPh, 42, 3
Schroeter, E. H., & Woehl, H. 1976, SoPh, 49, 19
Schroeter, E. H., Woehl, H., Soltau, D., & Vazquez, M. 1978, SoPh, 60, 181
Schwan, H., & Woehl, H. 1978, A&A, 70, 297
Sheeley, N. R. J., Cooper, T. J., & Anderson, J. R. L. 2011, ApJ, 730, 51
Singh, J., Priyal, M., Sindhuja, G., & Ravindra, B. 2018, in IAU Symp. 340,
   Long-term Datasets for the Understanding of Solar and Stellar Magnetic
  Cycles, ed. D. Banerjee et al. (Cambridge: Cambridge Univ. Press), 23
Skokić, I., Brajša, R., Roša, D., Hržina, D., & Wöhl, H. 2014, SoPh, 289
  1471
Snodgrass, H. B., & Howard, R. 1985, SoPh, 95, 221
Snodgrass, H. B., & Ulrich, R. K. 1990, ApJ, 351, 309
Spoerer, F. W. G. 1889, AN, 121, 105
Strassmeier, K. G., & Bopp, B. W. 1992, A&A, 259, 183
Sudar, D., Skokić, I., Brajša, R., & Saar, S. H. 2015, A&A, 575, A63
Suzuki, M. 2014, SoPh, 289, 4021
Temmer, M., Rybák, J., Bendík, P., et al. 2006, A&A, 447, 735
Tlatov, A. G., Pevtsov, A. A., & Singh, J. 2009, SoPh, 255, 239
Ulrich, R. K., Evans, S., Boyden, J. E., & Webster, L. 2002, ApJS, 139, 259
Waldmeier, M. 1971, SoPh, 20, 332
Weiss, N. O., & Tobias, S. M. 2000, SSRv, 94, 99
Zhang, L., Mursula, K., & Usoskin, I. 2013, A&A, 552, A84
```